

# Picosecond Spin Orbit Torque Switching

Kaushalya<sup>1</sup>, Julius Hohlfeld<sup>1</sup>, Akshay Pattabi<sup>2</sup>, Elodie Martin<sup>1</sup>, Aldo Ygnacio Arriola Córdova<sup>1,3</sup>, Xinping Shi<sup>4</sup>, Roberto Lo Conte<sup>3</sup>, Sébastien Petit-Watelot<sup>1</sup>, Juan Carlos Rojas-Sánchez<sup>1</sup>, Gregory Malinowski<sup>1</sup>, Stéphane Mangin<sup>1</sup>, Aristide Lemaître<sup>5</sup>, Michel Hehn<sup>1</sup>, Jeffrey Bokor<sup>2,6</sup>, Richard B. Wilson<sup>4</sup>, Jon Gorchon<sup>1,\*</sup>

Reducing energy dissipation while increasing speed in computation and memory is a long-standing challenge for spintronics research<sup>1</sup>. In the last 20 years, femtosecond lasers have emerged as a tool to control the magnetization in specific magnetic materials at the picosecond timescale<sup>2–4</sup>. However, the use of ultra-fast optics in integrated circuits and memories would require a major paradigm shift. An ultrafast *electrical* control of the magnetization is far preferable for integrated systems. Here we demonstrate reliable and deterministic control of the out-of-plane magnetization of a 1 nm-thick Co layer with single 6 ps-wide electrical pulses that induce spin orbit torques on the magnetization. We can monitor the ultrafast magnetization dynamics due to the spin orbit torques on sub-picosecond timescales, thus far accessible only by numerical simulations. Due to the short duration of our pulses, we enter a counter-intuitive regime of switching where heat dissipation assists the reversal. Moreover, we estimate a low energy cost to switch the magnetization, projecting to below 1fJ for a (20 nm)<sup>3</sup> cell. These experiments prove that spintronic phenomena can be exploited on picosecond time-scales for full magnetic control and should launch a new regime of ultrafast spin torque studies and applications.

There is a largely held belief, that switching the magnetization of a system coherently in less than half of its natural precessional period (i.e. its ferromagnetic resonance) is impossible<sup>5,6</sup>. However, if a strong enough effective field is induced, due to a strong spin injection for example, the LLG equation that governs the magnetization dynamics does predict switching. Currently, the spin-transfer torque (STT) effect<sup>7</sup>, a magnetization torque due to spin-polarized current injection, is the mechanism of choice for the control of the magnetic layer in magnetic random access memories. However, the reversal speed is still limited to the nanosecond (ns) regime<sup>8</sup>. As current pulses become shorter, higher peak values are required for STT-based technologies, which may damage the tunnel barriers that are used for readout. Since 2011, novel mechanisms relying on high spin-orbit materials in order to convert charge currents into transverse spin currents have flourished<sup>9,10</sup> as a promising alternative to STT, in part because the switching current would not need to cross the tunnel barrier. Moreover, these so called *spin-orbit torques* (SOT) offer an interesting trade-off of a small reduction in areal density for increases in speed, energy efficiency, reliability and endurance. In particular, due to the orthogonality of the injected spin with respect to the magnetization in perpendicularly magnetized films, the switching process starts instantaneously leading to a sub-ns switching that is fully deterministic<sup>11</sup>.

In order to further increase the speed of the reversal, below the 200 ps barrier<sup>11–13</sup>, and explore the magnetization dynamics and energy requirements in such fast regimes, new techniques are required. On the one hand commercial pulse generators with such bandwidth are scarce and expensive or even nonexistent below the 50ps duration. On the other hand, picosecond-ready CMOS exists since 2007<sup>14</sup>. Therefore, if methods for using picosecond electrical pulses and SOT to control magnetic order are developed, these methods have the potential to be integrated into ultrafast electronic devices.

To investigate picosecond SOT phenomena, we use an experimental platform that uses photoconductive switches<sup>15</sup> to generate picosecond electrical pulses. We recently used such devices to demonstrate energy-efficient reversal of the magnetization of a GdFeCo thin-film with a sub-10ps electrical pulse<sup>16</sup>. However, the switching mechanism in GdFeCo relies on ferrimagnetic order and is therefore not generalizable to most magnetic materials. The magnetic moment of GdFeCo toggles back and forth on repeated pulses independent of the current polarity due to the effects of rapid Joule heating<sup>16,17</sup>. For application purposes one would rather have a mechanism in which the final state depends on the polarity of the current, and ideally be able to extend the range of compatible materials. Here, we generate and inject 6 ps-wide electrical pulses to trigger SOT dynamics in a prototypical thin Co magnetic film, leading to ultrafast magnetization dynamics and a complete reversal of the moment.

We grew a Ta(5nm)/Pt(4)/Co(1)/Cu(1)/Ta(4)/Pt(1) stack (shown in Figure 1.a, with thicknesses in nm) on both glass and GaAs substrates (see methods). The Co layer had perpendicular magnetic anisotropy, as shown by the anomalous Hall effect measurement in Figure 1.c. The bottom Pt and top Ta were chosen for their opposite signs of spin Hall angles, in order to enhance the torques on the Co layer<sup>18</sup>. We fabricated the Hall structures shown in Figure 1.b, and performed field driven (Figure 1.c) and current driven (Figure 1.d) hysteresis by monitoring the Hall resistance. Current experiments used 100  $\mu$ s pulses under an applied in-plane applied field  $H_x$ . We find that the critical current density  $J_c$  is equal to  $\sim 2 \cdot 10^{11} \text{ A/m}^2$  for a 160 mT field, and is inversely proportional to the in-plane field accordingly to

<sup>1</sup>Université de Lorraine, CNRS, IJL, F-54000 Nancy, France <sup>2</sup>Department of Electrical Engineering and Computer Sciences, University of California, Berkeley, CA 94720, USA <sup>3</sup>Universidad Nacional de Ingeniería, Avenida Túpac Amaru 210, Rímac, Lima, Perú <sup>4</sup>Department of Mechanical Engineering and Materials Science and Engineering Program, University of California, Riverside, CA 92521, USA <sup>5</sup>Centre de Nanosciences et de Nanotechnologies (C2N), CNRS, Université Paris Sud, Université Paris-Saclay, 91120 Palaiseau, France <sup>6</sup>Lawrence Berkeley National Laboratory, 1 Cyclotron Road, Berkeley, CA 94720, USA  
\*e-mail: [jon.gorchon@univ-lorraine.fr](mailto:jon.gorchon@univ-lorraine.fr)

SOT-driven switching (see supp. mat.). The sample switches to  $-M_z$  ( $+M_z$ ) when the in-plane field and current pulses are parallel (antiparallel), in agreement with a SOT rising from the combination of the spin Hall effect from both heavy metals<sup>19,20</sup>.

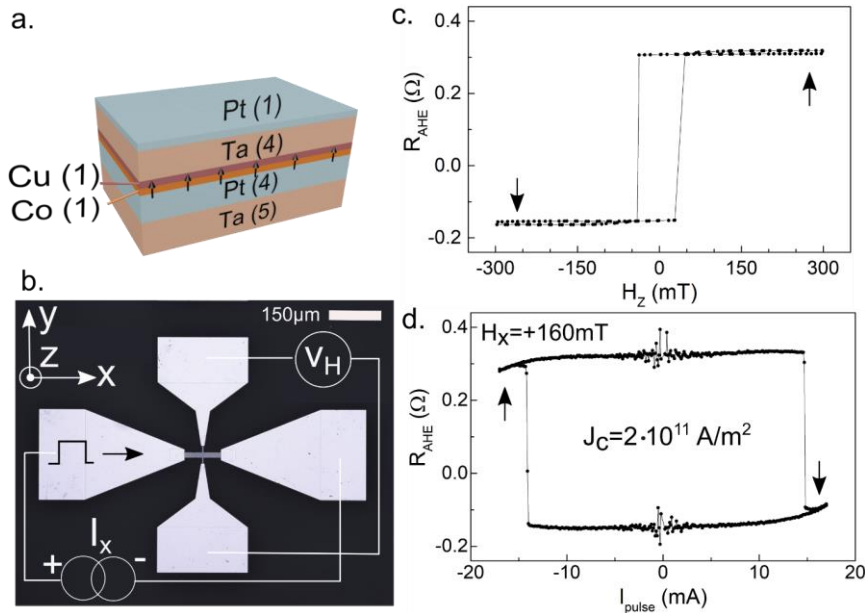


**Figure 1: Sample and switching behavior via field and current.** a) Magnetic sample stack b) Patterned Hall bar using the magnetic stack and gold contact pads. The schematic shows the electrical connections used for Anomalous Hall resistance ( $R_{AHE} = V_H/I$ ) detection as a function of c) out-of-plane magnetic field ( $H_z$ ) and d) 100  $\mu$ s current pulses under a 160mT in-plane field ( $H_x$ ).

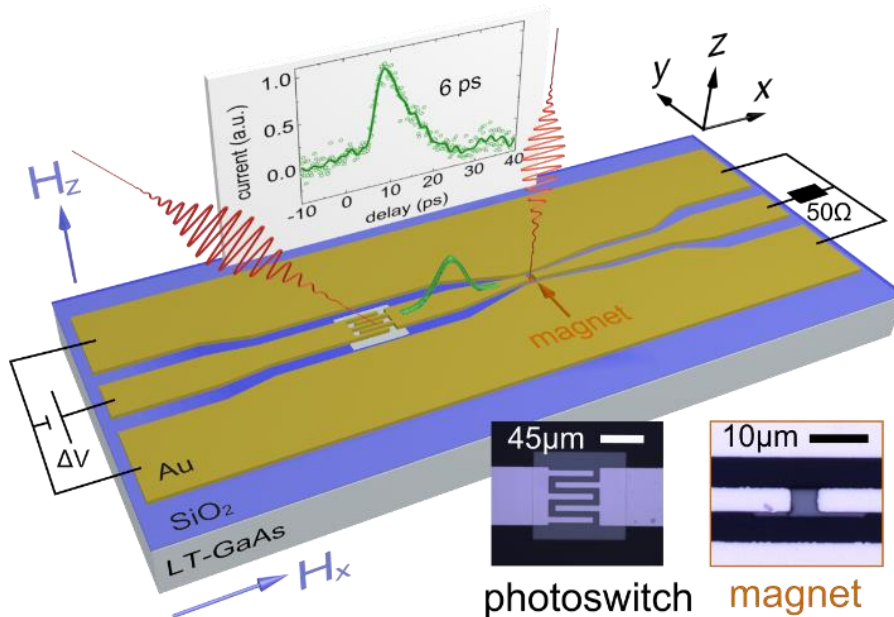


**Figure 2: Setup for generation of picosecond electrical pulses and magneto-optical detection.** The optical pump excites the photoconductive switch in order to generate  $\sim$ 6 ps duration electrical pulses, that are guided and focused by a coplanar waveguide into the magnetic stack, resulting in ultrafast spin orbit torques. The sampled picosecond current pulse is shown on the back of the figure. The solid green line is a guide for the eyes.

We use low-temperature GaAs (LT-GaAs) photoconductive switches to generate picosecond pulses of high intensity<sup>15</sup> (shown in Figure 2, see methods for sample fabrication and pulse generation details). In order to generate high current pulses we excite the switches with

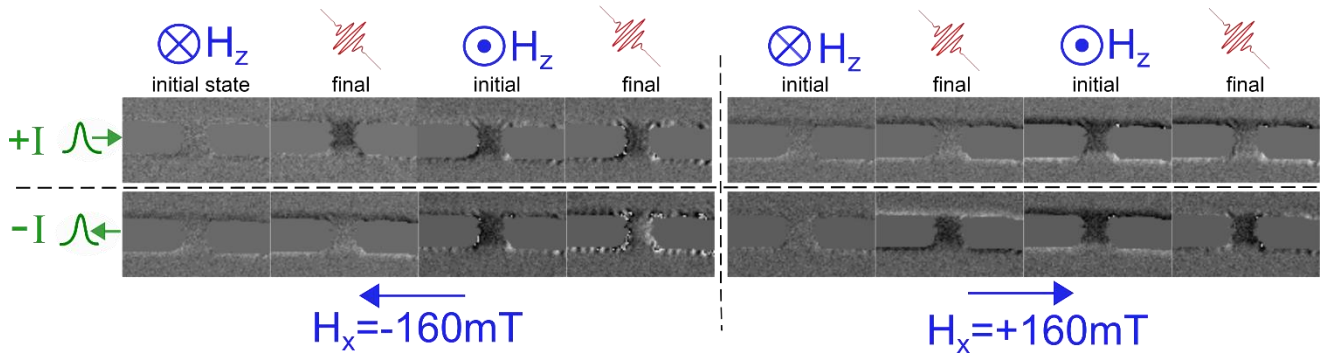


**Figure 3: MOKE micrographs of single 6 ps electrical pulses switching the magnetization via SOT.** The four quadrants show 2 before and 2 after-pulse images under different in-plane field and current directions. The inversion of the final state with current or in-plane field is a clear signature of SOT switching. Bias voltages used for switching were slightly above the critical threshold ( $\Delta V \sim 40$  V).

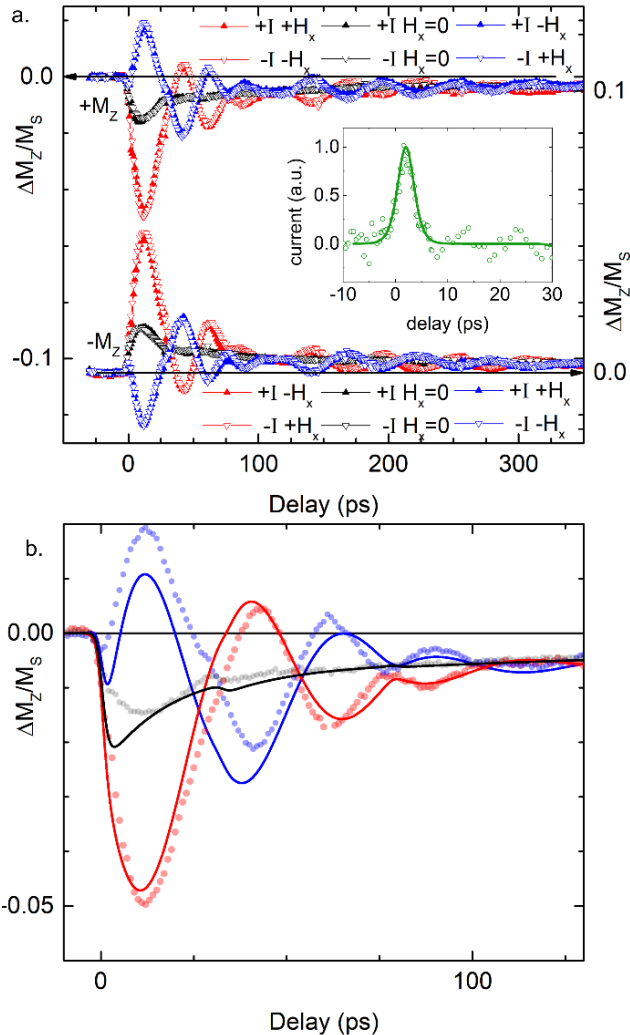
an amplified 5 kHz repetition rate laser system with 30 fs pulses centered at 800 nm. The use of this laser system with our photoswitches results in 6 ps duration ( $\tau_p$ ) high intensity current pulses (shown in the graph of Figure 2). We measure the pulse duration with a Teraspike® free-standing electric field detector (see methods). After excitation, the electrical pulses propagate (see Figure 2) on Au coplanar waveguides and are focused into the magnetic structure by an impedance matched tapper.

Figure 3 shows polar magneto optical Kerr effect (pMOKE) micrographs of the initial and final states after a single 6ps electrical pulse in various configurations. The final state is the same regardless of the initial *down* (bright contrast) or *up* (dark contrast) state of the magnet. In each of the four quadrants of Figure 3 we test combinations of current and in-plane field directions. Again, we observe that parallel (antiparallel) current pulses and field result in  $-M_z$  ( $+M_z$ ), just as expected by the symmetries of the SOTs in the prepared stack. We injected up to 10 pulses and saw no difference in the final state. We repeated the experiment at least 10-20 times confirming the deterministic behavior of the reversal. When the in-plane field was reduced below ( $H_x \sim 120$  mT) no more reversal was observed, likely requiring higher current densities, as also observed by Garello et al.<sup>11</sup>. The magnetic structures were exposed to the 5kHz laser at switching conditions for hours ( $> 10^8$  cycles) with no noticeable degradation of the switching behavior or magnetic properties of the stack. To confirm repeatability, we conducted additional switching measurements on a different set of photoconductive devices (including different waveguide and switch designs). We observed similar switching characteristics in these separate devices.

To measure the ultrafast magnetic response to the current pulses, we performed time-resolved MOKE measurements under various configurations of current polarity and magnetic fields. We were unable to obtain time-resolved switching dynamics due to technical limitations (see supp. mat.). We therefore performed low intensity time-resolved studies with an 80 MHz oscillator laser with  $\sim 250$  fs-duration pulses centered at 780 nm (see methods). With this system we obtain 3.7 ps-duration electrical pulses (inset in Figure 4.a). In these experiments, we monitor the out-of-plane component of the magnetization ( $\Delta M_z$ ) via pMOKE with a time-delayed probe pulse. The typical magnetic response to the pulses is shown in Figure 4.a.

The response of the Co magnetization to the current appears instantaneous, indicating the response time to SOT is faster than the picosecond temporal resolution of our pump/probe (see methods for time-delay calibration). At zero in-plane field we observe a response that closely resembles an ultrafast demagnetization<sup>17,21</sup>. However, there should be spin torques present as well that affect the detected  $\Delta M_z$ . We attribute the offset and slow recovery at long delays (at 350 ps) to the change in magnetization and/or anisotropy due to ultrafast Joule heating<sup>17</sup>. The addition of an in-plane field breaks the symmetry of the system and determines the sign for the observed coherent precession. When we change the direction of the bias voltage or the in-plane field  $H_x$ , the initial torque (first oscillation) acting on the magnetization changes sign, as is expected for SOT. A parallel (antiparallel) field and current (i.e. voltage) initially torques the magnetization towards  $-M_z$  ( $+M_z$ ), regardless of initial up or down state, in perfect agreement with the result of our quasi-static SOT switching experiments from Figure 1.d. The rapid precessions are offset by the demagnetization response, which in some configurations enhances the  $\Delta M_z$  and in others decreases it. We note that ultrafast demagnetization of an out-of-plane magnetized sample under an in-plane field (here  $H_x$ ) induces an ultrafast anisotropy torque. The anisotropy torque is due to the rapid heating of the magnet and decrease of the anisotropy field, and is thus independent of the direction of the current, and always torques the magnet towards the opposite out-of-plane direction. This effect is therefore part of the asymmetry in amplitude between the blue and red curves in Figure 4.a and is assisting the SOT in the switching of the magnetization.

We developed a simple macrospin model where we included SOT torques and ultrafast demagnetization (for details see suppl. mat.). The model assumes simplistic temperature dependence laws for the anisotropy and magnetization to calculate the anisotropy torques. We set the spin Hall angle to 0.3 from Ref<sup>22</sup>,  $M_s$  from VSM measurements and the damping and anisotropy at room temperature from optical pump-probe experiments. We also had to include a number of electrical reflections of the current pulses from the end of the transmission lines which affect the dynamics. The resulting best fits are shown in Figure 4.b. The quality of the fit is remarkable for such a simple model. However, we do miss some features, in particular the initial dynamics of the black trace at  $H_x=0$  and the amplitude of the blue curve. The fits indicate a fully damping-like torque dominated dynamics, in agreement with reports on similar structures<sup>22</sup>. Preliminary simulations at higher currents confirm the importance of heating for switching (see suppl. mat.).



**Figure 4: Time-resolved MOKE response due to a 3.7ps electrical pulse and macrospin simulation.** a) The dynamics include spin orbit torques and thermal effects (demagnetization). The phase and sign of the torques is dependent on the in-plane field ( $H_x$ ) and current direction, as expected from SOT. Without the symmetry-breaking in-plane field the oscillations disappear. The solid green line is a fit of current trace with a sech<sup>2</sup> function of 3.7ps (FWHM). Experiments were done after  $\pm M_z$  saturation of the sample, under  $H_z = 0$  mT,  $H_x = \pm 160$  mT and a bias voltage of  $\Delta V \sim 30$  V. b) Macrospin simulation (lines) including ultrafast demagnetization and SOTs on top of the  $+M_z$  data (circles).

We set an upper limit to the energy dissipated at the load by estimating the total initial energy stored in the photoswitch capacitor, which is the energy that drives both the THz current pulse in the lines and the losses to THz radiation<sup>23-25</sup>. We estimate the maximum capacitance of the switch to  $C_{max} \sim 74$  fF (see methods), and for the measured bias voltage at the switching threshold voltage of  $\Delta V = 40$  V, the energy stored is  $\frac{1}{2} C_{max} \Delta V^2 \sim 60$  pJ. In a worst case scenario, if we assume a full discharge of the switch, no radiative losses, no

transmission losses and assume a perfect absorption at the magnet, then all of the energy stored in the switch capacitor would be dissipated at the load. For our magnetic load, this corresponds to an energy density of  $\sim 180 \text{ MJ/m}^3$ . Because the energy dissipation for a Gaussian current pulse is  $E = \int J(t)^2 \rho \cdot dt = 0.75 \cdot J^2 \rho \tau_p$ , where  $\rho$  ( $= 81 \mu\Omega \cdot \text{cm}$ ) is the measured resistivity of the magnet, we estimate the maximum peak current density for switching with  $\tau_p = 6 \text{ ps}$  pulses to be about  $J_c \sim 7 \cdot 10^{12} \text{ A/m}^2$ .

The energy requirements in this ultrafast SOT regime compares extremely favorably with state of the art, ns and sub-ns switching SOT results<sup>12,13,26</sup> and other types of memory<sup>26</sup>, even though we are using a non-optimized stack with  $\mu\text{m}$  dimensions. The energy per bit, assuming an ideal scaling down to  $(20 \text{ nm})^3$  would be below  $\sim 1 \text{ fJ}$ . As an example, we can compare the estimated **74** pJ of energy dissipation in our  $\sim 5 \times 4 \mu\text{m}^2$  devices to state-of-the-art values such as Garello's<sup>12</sup> 300 pJ in a  $\sim 62 \times 62 \text{ nm}^2$  devices or Zhu's<sup>13</sup> 14 pJ in a  $190 \times 45 \text{ nm}^2$  highly optimized stack.

Switching via a spin (orbit) torque on such a fast timescale brings up interesting questions about the mechanisms involved. For long pulses it is well known that thermal activation plays an important role in the nucleation of reversed magnetic domains, which followed by domain wall allows for switching, even in nanoscale devices<sup>20</sup>. Below the nanosecond, when we are typically below the ferromagnetic resonance period, thermal activation becomes negligible and we enter a deterministic switching regime<sup>11,12,27</sup>. Garello et al.<sup>11</sup> showed that switching in their  $\sim 100 \text{ nm}$  sized devices was still dominated by domain wall motion with sub-ns pulses. If we made the same analysis in our devices, due to the  $\mu\text{m}$  dimensions of our magnets and ps length of our pulses, it would imply unphysical  $10^5 \text{ m/s}$  domain wall velocities. This scenario is highly unlikely when considering the observed<sup>28</sup> and predicted<sup>29</sup> trends in domain wall velocities with current density. In order to check for a signature of non-coherent switching, we performed low intensity time-resolved dynamics (as in Figure 4.a) at various positions on the magnet with our  $\sim 1.5 \mu\text{m}$  diameter probe and found negligible differences (see methods).

Another possible scenario would be to consider some form of heat-assisted magnetic recording due to Joule heating. In such scenario the anisotropy barrier and/or magnetic order would be completely reduced by heating up to the Curie temperature  $T_c$  and any tiny torque could then determine the switching direction. However, we can quickly eliminate this scenario as we know that we do not reach  $T_c$  in our experiments (see suppl. mat.).

Therefore, our experiments, simulations and analysis tend to indicate that the switching is likely a coherent process driven by the combination of SOTs and anisotropy torques. The anisotropy torques arising from heat and assisting the SOT during the switching could be one of the reasons for the low switching energy.

In conclusion, we have demonstrated spin orbit torque switching of a thin Co film with a single 6 ps electrical pulse. We show that picosecond-duration electrical pulses can inject spin into a magnet at ultrafast timescales. We can then probe the generated magnetization torques with picosecond resolution. All our experiments are in agreement with the symmetries expected from SOT. Macrospin simulations can accurately predict the observed dynamics, showing a damping-like torque dominated effect. Finally, we have shown that the reversal process is extremely energy efficient. Future work will include tracking different components of the magnetization via different magneto-optical effects, in order to spatially reconstruct the time-dependent spin torque dynamics. We believe our approach will trigger new interest in ultrafast electrical studies of spin torque dynamics, opening the door for the possible observation of elusive phenomena such as inertial dynamics in ferromagnetic materials<sup>30-32</sup> and offer a new way of triggering resonant dynamics in antiferromagnetic materials<sup>33,34</sup>.

## References

1. Åkerman, J. Toward a universal memory. *Science*. **308**, 508–510 (2005).
2. Radu, I. et al. Transient ferromagnetic-like state mediating ultrafast reversal of antiferromagnetically coupled spins. *Nature* **472**, 205–208 (2011).
3. Stupakiewicz, A., Szerenos, K., Afanasiev, D., Kirilyuk, A. & Kimel, A. V. Ultrafast nonthermal photo-magnetic recording in a transparent medium. *Nature* **542**, 71–74 (2017).
4. Kirilyuk, A., Kimel, A. V & Rasing, T. Ultrafast optical manipulation of magnetic order. *Rev. Mod. Phys.* **82**, (2010).
5. Olejník, K. et al. Terahertz electrical writing speed in an antiferromagnetic memory. *Sci. Adv.* **4**, 1–9 (2018).
6. Manchon, A. et al. Current-induced spin-orbit torques in ferromagnetic and antiferromagnetic systems. arXiv:1801.09636 (2018).
7. Stiles, M. & Zangwill, A. Anatomy of spin-transfer torque. *Phys. Rev. B* **66**, 014407 (2002).
8. Sato, H. et al. 14ns write speed 128Mb density Embedded STT-MRAM with endurance>10 10 and 10yrs retention@85°C using novel low damage MTJ integration process. *Int. Electron Devices Meet. IEDM 2018-Decem*, 27.2.1-27.2.4 (2019).
9. Miron, I. M. et al. Perpendicular switching of a single ferromagnetic layer induced by in-plane current injection. *Nature* **476**, 189–193 (2011).
10. Liu, L. et al. Spin-Torque Switching with the Giant Spin Hall Effect of Tantalum. *Science*. **336**, 555–558 (2012).

11. Garello, K. *et al.* Ultrafast magnetization switching by spin-orbit torques. *Appl. Phys. Lett.* **105**, 1–12 (2014).
12. Garello, K. *et al.* SOT-MRAM 300MM Integration for Low Power and Ultrafast Embedded Memories. in *2018 IEEE Symposium on VLSI Circuits* **54**, 81–82 (IEEE, 2018).
13. Zhu, L., Zhu, L., Shi, S., Ralph, D. C. & Buhrman, R. A. Energy-efficient ultrafast SOT-MRAMs based on low-resistivity spin Hall metal Au0.25Pt0.75. *arXiv:1910.11896*
14. Mistry, K. *et al.* A 45nm Logic Technology with High-k+ Metal Gate Transistors, Strained Silicon, 9 Cu Interconnect Layers, 193nm Dry Patterning, and 100% Pb-free Packaging. *Proc. IEDM* 247–250 (2007).
15. Auston, D. H., Johnson, A. M., Smith, P. R. & Bean, J. C. Picosecond optoelectronic detection, sampling, and correlation measurements in amorphous semiconductors. *Appl. Phys. Lett.* **37**, 371 (2008).
16. Yang, Y. *et al.* Ultrafast magnetization reversal by picosecond electrical pulses. *Sci. Adv.* **3**, e1603117 (2017).
17. Wilson, R. B. *et al.* Electric current induced ultrafast demagnetization. *Phys. Rev. B* **96**, 045105 (2017).
18. Woo, S. *et al.* Enhanced spin-orbit torques in Pt / Co / Ta heterostructures Enhanced spin-orbit torques in Pt / Co / Ta heterostructures. *Appl. Phys. Lett.* **105**, 212404 (2014).
19. Liu, L., Lee, O., Gudmundsen, T., Ralph, D. & Buhrman, R. A. Current-Induced Switching of Perpendicularly Magnetized Magnetic Layers Using Spin Torque from the Spin Hall Effect. *Phys. Rev. Lett.* **109**, 096602 (2012).
20. Baumgartner, M. *et al.* Spatially and time-resolved magnetization dynamics driven by spin-orbit torques. *Nat. Nanotechnol.* **12**, 980–986 (2017).
21. Beaurepaire, E., Merle, J.-C., Daunois, A. & Bigot, J.-Y. Ultrafast spin dynamics in ferromagnetic nickel. *Phys. Rev. Lett.* **76**, 4250–4253 (1996).
22. Woo, S., Mann, M., Tan, A. J., Caretta, L. & Beach, G. S. D. Enhanced spin-orbit torques in Pt/Co/Ta heterostructures. *Appl. Phys. Lett.* **105**, 212404 (2014).
23. Hoffmann, M. C. & Fülöp, J. A. Intense ultrashort terahertz pulses: Generation and applications. *J. Phys. D. Appl. Phys.* **44**, 083001 (2011).
24. Bonvalet, A. & Joffre, M. Terahertz Femtosecond Pulses. in *Femtosecond Laser Pulses* (ed. Rullière, C.) 309–333 (Springer, 2005).
25. Gregory, I. S. *et al.* Optimization of photomixers and antennas for continuous-wave terahertz emission. *IEEE J. Quantum Electron.* **41**, 717–728 (2005).
26. H.-S. P. Wong, C. Ahn, J. Cao, H.-Y. Chen, S. W. Fong, Z. Jiang, C. Neumann, S. Qin, J. Sohn, Y. Wu, S. Yu, X. Zheng, H. Li, J. A. Incorvia, S. B. Eryilmaz, K. O. Standford Memory Trends. Available at: <https://nano.stanford.edu/stanford-memory-trends>. (Accessed: 11th November 2019)
27. Cubukcu, M. *et al.* Ultra-Fast Perpendicular Spin–Orbit Torque MRAM. *IEEE Trans. Magn.* **54**, 1–4 (2018).
28. Miron, I. M. *et al.* Fast current-induced domain-wall motion controlled by the Rashba effect. *Nat. Mater.* **10**, 419–23 (2011).
29. Thiaville, A., Rohart, S., Jué, É., Cros, V. & Fert, A. Dynamics of Dzyaloshinskii domain walls in ultrathin magnetic films. *Europhys. Lett.* **100**, 57002 (2012).
30. Kikuchi, T. & Tataro, G. Spin dynamics with inertia in metallic ferromagnets. *Phys. Rev. B* **92**, 1–15 (2015).
31. Wegrowe, J.-E. & Ciornei, M.-C. Magnetization dynamics, gyromagnetic relation, and inertial effects. *Am. J. Phys.* **80**, 607–611 (2012).
32. Neeraj, K. *et al.* Experimental evidence of inertial dynamics in ferromagnets. *arXiv:1910.11284* 1–10 (2019).
33. Němec, P., Fiebig, M., Kampfrath, T. & Kimel, A. V. Antiferromagnetic opto-spintronics. *Nat. Phys.* **14**, 229–241 (2018).
34. Baltz, V. *et al.* Antiferromagnetic spintronics. *Rev. Mod. Phys.* **90**, 15005 (2018).
35. Nan, T. *et al.* Comparison of spin-orbit torques and spin pumping across NiFe/Pt and NiFe/Cu/Pt interfaces. *Phys. Rev. B* **91**, (2015).
36. Ostwal, V., Penumatcha, A., Hung, Y. M., Kent, A. D. & Appenzeller, J. Spin-orbit torque based magnetization switching in Pt/Cu/[Co/Ni]5 multilayer structures. *J. Appl. Phys.* **122**, (2017).
37. Pham, T. H. *et al.* Thermal Contribution to the Spin-Orbit Torque in Metallic-Ferrimagnetic Systems. *Phys. Rev. Appl.* **9**, 1–9 (2018).
38. Burford, N. M. & El-Shenawee, M. O. Review of terahertz photoconductive antenna technology. *Opt. Eng.* **56**, 010901 (2017).
39. Gupta, K. C., Ramesh, G., Bahl, I. & Bhartia, P. *Microstrip Lines and Slotlines*. (1996).
40. Lo Conte, R. *et al.* switching and thermal effects studied in Ta \ CoFeB \ MgO nanowires. *Appl. Phys. Lett.* **105**, 122404 (2015).

## Acknowledgments

We would like to thank Emmanuel Vatoux, Tom Ferté and both Laurent Badie and Gwladys Lengaigne for the electromagnet construction, VSM measurements and sample preparation, respectively. We would like to specially thank Yang Yang and Charles-Henri Lambert for their help in the first SOT switching trials years ago. This work was supported by the impact project LUE-N4S part of the French PIA project “Lorraine Université d’Excellence”, reference ANR-15IDEX-04-LUE and the “FEDER-FSE Lorraine et Massif Vosges 2014-2020”, a European Union Program. This work was also partly supported by the French RENATECH network. R.L.C. and J.B. gratefully acknowledge support from the National Science Foundation (NSF) through the Cooperative Agreement Award EEC-1160504 for Solicitation NSF 11-

537 (TANMS). A.P. and J.B. also gratefully acknowledge support from the NSF Center for Energy Efficient Electronics (E3S). Work by X. S. and R. W. was supported by the U.S. Army Research Laboratory and the U.S. Army Research Office under contract/grant number W911NF-18-1-0364.

## Author contributions

J.G. designed the experiments with inputs from R.B.W, J.B, S.P-W. & J.H. A.L. grew the LT-GaAs substrates. M.H. optimized and grew the samples by sputtering. K. fabricated the devices. K., J.H. and J.G., performed the ultrafast SOT experiments and characterized the picosecond pulses. E.M., A.Y.A.C. performed the anomalous Hall measurements and 100 $\mu$ s SOT switching experiments under the supervision of J.C.R.S. and S.P-W. who designed the mask and set up this experiment. R.B.W. built the numerical model and performed the simulations with inputs from J.G. R.B.W. performed optical time-resolved experiments to determine the damping and anisotropy of the samples. J.G. analyzed the experimental data with help from K., R.B.W., R.L.C., J.H. and S-P.W. J.G. wrote the manuscript with input from all authors.

## Competing financial interests

The authors declare no competing financial interests.

## Methods

### Samples

The LT GaAs substrate was obtained by first depositing, in a molecular beam epitaxy chamber, at high temperature (550°C) a 300 nm thick GaAl<sub>0.8</sub>As buffer followed by a 5nm thick GaAs layer on a semi-insulating GaAs (100) substrate. Then the LT GaAs layer (1  $\mu$ m thick) was deposited at 260°C with a As/Ga beam equivalent pressure ratio of 50.

The magnetic stacks were grown by DC magnetron sputtering in an AJA system. The Ta(5nm)/Pt(4) buffer layer ensures a well-defined (111) texture for the growth of Co(1) and guarantees an interface anisotropy that promotes PMA for Co(1). The Cu(1)/Ta(4) bilayer, capped by Pt(1) to prevent Ta oxidation, has been added to preserve PMA and enhance the torques on the Co layer since Pt and Ta have spin Hall angles with opposite sign. The Cu was inserted to reduce the Dylazosinkii-Moriya interaction at the top Co interface in order to optimize the coercive field and PMA and obtain two well-defined remanent states at zero field. Due to the long spin-diffusion length of Cu, spin currents generated in the Ta are expected to contribute to the SOT<sup>35,36</sup>. The choice of the stack was also determined by the necessity of having a top metallic layer (Cu/Ta + Pt capping) in order to get a good electrical contact with the transmission lines shown in **Figure 2**. The  $T_c$  of the sample is estimated as ~800 K due to previous experience with extremely similar samples grown and characterized in the group over the years.

The sample was fabricated using a 3 step-based UV-lithography technique where the SiO<sub>2</sub> layer, magnetic load, and transmission lines were patterned at each step. The SiO<sub>2</sub> layer allows for a good insulation of the transmission lines from the substrate in order to suppress leakage currents. A single recipe was used to perform lithography and lift-off for all three steps. An AC 450 (Alliance Concept) sputtering system was used to deposit 100 nm of SiO<sub>2</sub> in the presence of 20sccm Ar and O<sub>2</sub> flow at a base pressure of 6.1×10<sup>-3</sup> mbar. E-beam evaporation was used to deposit Ti(20 nm)/Au(300 nm) for the transmission lines. The coplanar waveguide has a center-line to side-line distance of 60  $\mu$ m. The waveguides have a 60  $\mu$ m-wide center-line, that tapers down to a 5.5  $\mu$ m spaced 4  $\mu$ m-wide center-line, as depicted in Figure 2. The magnetic load is a 20  $\mu$ m x 4  $\mu$ m strips partially covered by the Au transmission lines, so current only flows through the magnetic stack only in the uncovered 5 x 4  $\mu$ m opening.

The Hall bars where patterned via similar lithography process, as published elsewhere<sup>37</sup>.

### Generation of picosecond-duration electrical pulses

In order to generate the picosecond pulses (schematic shown in **Figure 2**) we contact the left side of the transmission lines with a CPW 40GHz GBB® probe tip. We also contact the right side with another CPW 40GHz GBB® tip, and add a 50 $\Omega$  resistor to close the circuit. We apply a constant voltage bias ( $\Delta V$ ) through the left tip between -50V and +50V via a Keithley 2400 voltage source, while reading the average current. If no laser irradiation is incident, we can measure a dark (i.e. leakage) current due to the finite switch resistance (>10 M $\Omega$ ). We then irradiate the photoswitch with either 1.5mW (0.3  $\mu$ J per pulse) from our 5kHz amplified laser or 30mW (0.37 nJ per pulse) from the 80MHz oscillator system. The pump is focused by a 15 cm lens to a (FWHM) radius of about 150  $\mu$ m. When the switch is irradiated a photocurrent is generated, which we can then optimize by finely tuning the pump mirror. We note that photoswitch excitation with the high voltages and high pulse energies used for the switching experiments can result in longer electrical pulses durations (6 ps for switching experiments vs 3.7 ps for time-resolved experiments)<sup>38</sup>.

### Measurement of time-resolved dynamics

All the presented small-intensity dynamics were measured with the 80MHz oscillator laser system focused through a 50x objective into a  $\sim 1\mu\text{m}$  sized spot. The experiments were performed with no out-of-plane field, since at small excitations the sample naturally relaxed back between pulses, as is typical with low-excitation optical pump-probe experiments. We determined the zero delay time, i.e. the arrival of the electrical pulse, by monitoring the time-domain thermoreflectance (TDTR) response (see supp. mat.).

### Measurement of picosecond pulse electric field

A pump beam is focused on the photoconductive switch to generate the pulse. The pump beam is chopped by an optical chopper at about 300 Hz. We place the Teraspike® probe on top of the transmission lines. A probe beam is focused at the tip of Teraspike® probe, exciting the free-standing photoconductive switch. A Standford Research Systems 865A Lock-In amplifier is used to directly measure the change in current induced by the transient electric field at the tip of the probe. This change in current is only present when both the electric field and probe beams coincide in time. Therefore, changing the delay between optical pump and probes allows us to sample the transient electric field associated with the picosecond current pulses. The resulting trace is a convolution of the real electric field and the Teraspike®'s response. We note that we do not measure the electric pulse at the sample position.

### Estimation of switch capacitance

The capacitance of an interdigitated electrode (IDE) capacitor  $C_{IDE}$  is roughly  $C_{IDE} = (N - 1)\epsilon_r\epsilon_0 A/d$  where  $N$  is the number of electrodes,  $\epsilon_r$  is the effective relative permittivity due to LT-GaAs substrate and air (measured as 15),  $\epsilon_0$  is the vacuum permittivity,  $A$  is the surface area of an electrode and  $d$  is the center-to-center distance between electrodes. We estimate a capacitance of about  $\sim 1.7 \cdot 10^{-14}$  F for our photoconductive switch. As a second verification, it is also well known that the RC time constant due to the capacitance of the photoswitch limits the pulse duration of the generated pulses<sup>15</sup>, which means we can also set an upper bound for the capacitance given by  $RC < 3.7\text{ps}$  (which is our smallest measured pulse duration). Here, the characteristic impedance ( $Z_0$ ) of the line plays the role of the resistor. The CPW line impedance was designed<sup>39</sup> to be  $Z_0 = 50\Omega$ , which means the capacitance is at most around  $7.4 \cdot 10^{-14}$  F, consistent with our initial estimation. We will consider this upper-bound value as the capacitance of our switch to calculate the upper-bound energy dissipation in our experiments.

# Picosecond Spin Orbit Torque Switching

Kaushalya<sup>1</sup>, Julius Hohlfeld<sup>1</sup>, Akshay Pattabi<sup>2</sup>, Elodie Martin<sup>1</sup>, Aldo Ygnacio Arriola Córdova<sup>1,3</sup>, Xinping Shi<sup>4</sup>, Roberto Lo Conte<sup>3</sup>, Sébastien Petit-Watelot<sup>1</sup>, Juan Carlos Rojas-Sánchez<sup>1</sup>, Gregory Malinowski<sup>1</sup>, Stéphane Mangin<sup>1</sup>, Aristide Lemaître<sup>5</sup>, Michel Hehn<sup>1</sup>, Jeffrey Bokor<sup>2,6</sup>, Richard B. Wilson<sup>4</sup>, Jon Gorchon<sup>1,\*</sup>

## Supplementary materials:

1. Dependence of quasi-static critical current density on in-plane field
2. Estimation of resistivity and critical current density
3. Determination of zero-time delay from Time Domain Thermoreflectance
4. Time-resolved switching dynamics
5. HAMR-scenario and dependence of coercivity on number of pulses
6. Spatial dependence of magnetic dynamics
7. Macrospin model

---

<sup>1</sup>Université de Lorraine, CNRS, IJL, F-54000 Nancy, France <sup>2</sup>Department of Electrical Engineering and Computer Sciences, University of California, Berkeley, CA 94720, USA <sup>3</sup>Universidad Nacional de Ingeniería, Avenida Túpac Amaru 210, Rímac, Lima, Perú <sup>4</sup>Department of Mechanical Engineering and Materials Science and Engineering Program, University of California, Riverside, CA 92521, USA <sup>5</sup>Centre de Nanosciences et de Nanotechnologies (C2N), CNRS, Université Paris Sud, Université Paris-Saclay, 91120 Palaiseau, France <sup>6</sup>Lawrence Berkeley National Laboratory, 1 Cyclotron Road, Berkeley, CA 94720, USA

\*e-mail: [jon.gorchon@univ-lorraine.fr](mailto:jon.gorchon@univ-lorraine.fr)

### 1. Dependence of quasi-static critical current density on in-plane field

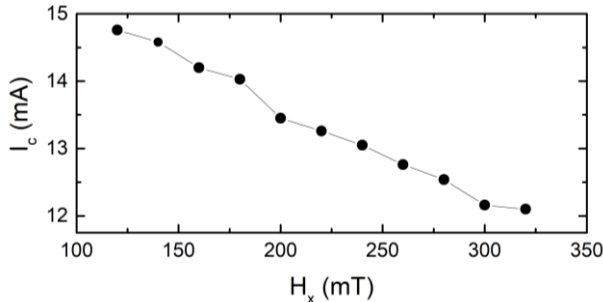


**Figure S1:** The critical current density for SOT switching with 100  $\mu$ s pulses is inversely proportional to the in-plane  $H_x$  field increases, as reported previously<sup>40</sup>.

### 2. Estimation of resistivity and quasi-static critical current density

A four point resistivity measurement yielded an effective resistivity of  $\rho = 81 \mu\Omega \cdot \text{cm}$ . Using previously measured values of resistivity for 4-5nm Pt and Ta films deposited with the same sputtering system (24 and 200  $\mu\Omega \cdot \text{cm}$  respectively), and a parallel resistor model, we find the correct effective resistivity by assuming that most of the current flows in the 13nm comprised by the 5nm Ta buffer, bottom 4nm Pt and top 4nm Ta layers, and neglecting the currents through the 1nm Co, Cu and Pt capping layers. We then estimate the critical current density by using again a parallel resistor model to determine the amount of current going through Pt and Ta layers surrounding the Co/Cu bilayer.

### 3. Determination of zero-time delay from Time Domain Thermoreflectance

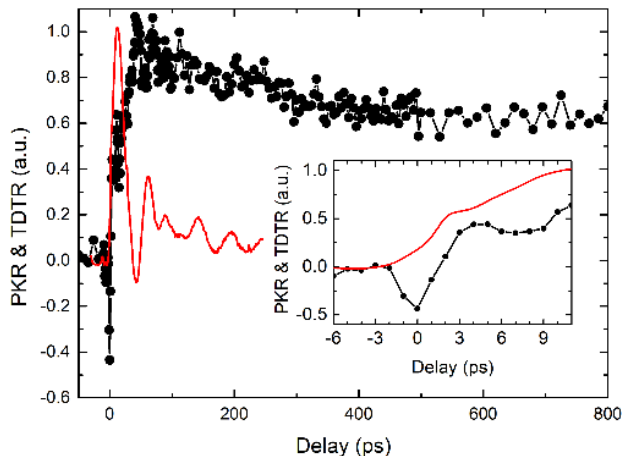


**Figure S2:** Time-domain thermoreflectance (TDTR) in black and polar MOKE (PKR) response in red. The TDTR allows us to set time-zero in our experiment. The electrons immediately respond to the heat pulse (negative peak at time-zero). The magnetic dynamics (red) equally start at the arrival of the pulse with no noticeable delay. Further work is needed to fully interpret the TDTR response.

### 4. Time-resolved switching dynamics

Time-resolved pump/probe measurements of the switching dynamics were not possible with our 5 kHz amplified laser system. On our MOKE setup measurements require a minimum probe power of  $\sim 60 \mu\text{W}$  is required to resolve Kerr rotations of  $\sim 100 \mu\text{rad}$ . The full amplitude of the hysteresis ( $2M_s$ ) measured with the 80MHz oscillator system, shown in **Figure S3** is  $\sim 485 \mu\text{rad}$ , so 60  $\mu\text{W}$  would allow us to resolve the dynamics with approximatively a SNR of less than approximately 5:1 (without accounting for drift issues). However, at a 5 kHz rep rate, the per pulse energy for 60  $\mu\text{W}$  causes damage to the sample when focused to sub-3  $\mu\text{m}$  dimensions.

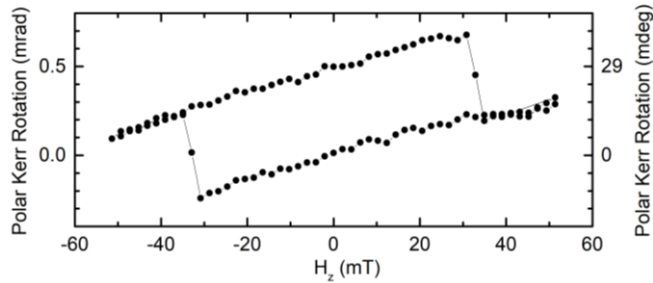


Figure S3: Polar MOKE hysteresis on the CPW-embedded magnetic sample taken with the 80MHz laser system.

### 5. HAMR-scenario and dependence of coercivity on number of pulses

In order to check for a heat assisted magnetic recording-like scenario, we injected single pulses at the switching threshold current, under no in-plane field, with an additional out-of-plane magnetic field  $H_z$  at  $\sim 93\%$  of the room temperature coercivity favoring switching. If the sample was to be heated near  $T_c$ , then any magnetic field would lead to reversal, lowering the effective coercivity dramatically. However, we did not observe any switching when injecting a single pulse under these conditions. In fact, we only observe a small decrease of  $\sim 30\%$  in the coercivity when increasing the number of pulses by a factor of  $10^5$  (see Figure S4). We conclude that the dissipation by the electrical pulse does not heat the Co film near  $T_c$ . We conclude that the dissipation by the electrical pulse does not heat the Co film near  $T_c$ .

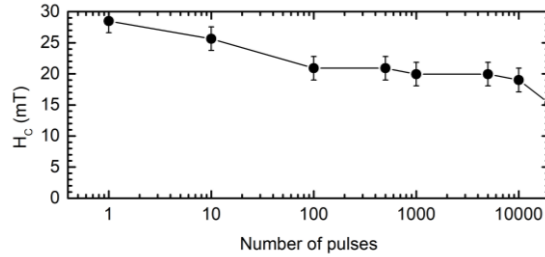


Figure S4: Coercivity as a function of the number of single 6ps pulses spaced every 200  $\mu$ s.

### 6. Spatial dependence of magnetic dynamics

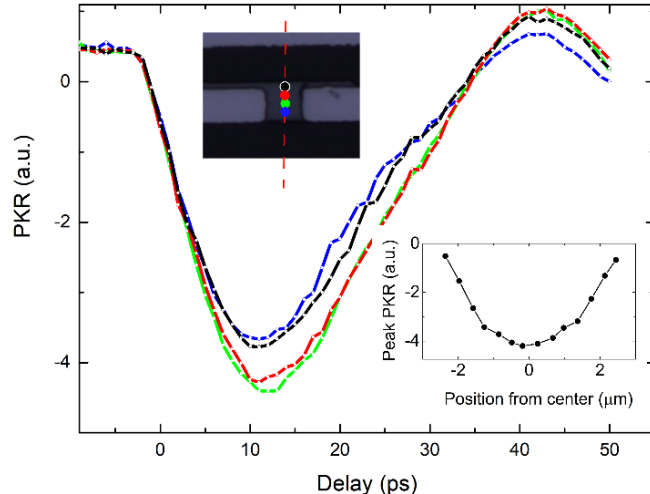


Figure S5: Spatial dependence of dynamics. Inset shows the peak (at 11ps) as a function of the y position (across the sample width). The signal drops as we get close to the edges because the probe no longer fully overlaps the magnet (the probe width is about 1.5  $\mu$ m (FWHM), and the sample width is 4  $\mu$ m. The dynamics are extremely similar across the surface of the sample. Experiments along the length of the magnet (x direction) also showed no major differences.

## 7. Macrospin model

### 7.1. Macrospin Simulations

To model the ability of picosecond electrical pulses to reverse the magnetization via spin orbit torques, we solve the Landau-Lifhitz-Gilbert equation of motion with anti-damping like and field-like damping terms from the spin-current. The equation of motion is

$$\frac{d\vec{M}}{dt} = -\gamma\mu_0(\vec{M} \times \vec{H}_{eff}) + \frac{\alpha}{M_s}(\vec{M} \times \frac{d\vec{M}}{dt}) - \frac{C_s}{M_s}(\vec{M} \times (\vec{M} \times \vec{\sigma})) + \beta C_s(\vec{M} \times \vec{\sigma}) \quad (\text{eq.S1})$$

where

$$C_s = \frac{\mu_B}{q_e} \frac{\theta_{SH} J_c}{d} \frac{1}{M_s} \quad (\text{eq.S2})$$

Here  $\gamma$  is the gyromagnetic ratio,  $\vec{\sigma}$  is the direction of spin-polarization. The effective field in the first and second term consists of a magneto-crystalline anisotropy field, a demagnetization field, and any applied external field,

$$\vec{H}_{eff} = -\frac{1}{\mu_0 M_s} \frac{\partial F}{d\vec{M}} = \begin{bmatrix} \vec{H}_x \\ \vec{H}_y \\ \vec{H}_z + \left( \frac{2K_z}{\mu_0 M_s} - M_s \right) \vec{m}_z \end{bmatrix} \quad (\text{eq.S3})$$

Here,  $\vec{H}_x$ ,  $\vec{H}_y$  and  $\vec{H}_z$  are the x, y, and z-components of the external field,  $K_z$  is the perpendicular anisotropy constant, and  $\vec{M} = M_s [\vec{m}_x \quad \vec{m}_y \quad \vec{m}_z]^T$ . The  $-M_s \vec{m}_z$  term in the z-direction is the demagnetization field due to thin-film shape anisotropy. In this work, we use the macrospin approximation, i.e. we assume the properties in Eq. (eq.S1) are independent of position.

To solve for the dynamics, we first set  $d\vec{M}/dt = 0$  and solve for the equilibrium orientation of the moment,  $\vec{M}(t < 0) = \vec{M}_0$ . We identify the stable solution to  $d\vec{M}/dt = 0$  by choosing the solution with the lowest free energy. We then use a finite-difference scheme to evolve  $\vec{M}(t)$  forward in time in response to a charge current  $J_c(t)$ . We evolve the magnetization forward in time with time-increments of  $\Delta t = 1$  fs. The current-densities required to move the magnetic moment of the Co layer into a new equilibrium orientation are shown in Fig. S6. Fig. S6 does not include the effects of temperature.

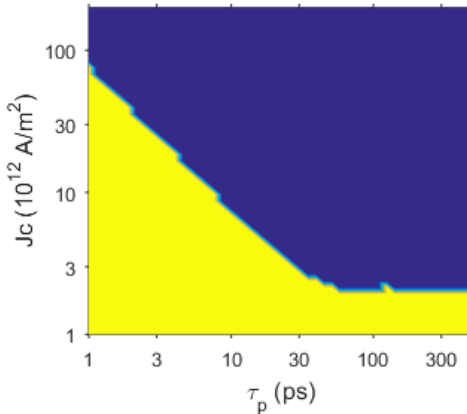


**Figure S6. LLG macrospin predictions for switching of a thin Co film in response to spin-orbit-torques.** We calculate  $\vec{M}(t)$  in response to  $J_c(t) = J_c f_{pulse}(t, \tau_p)$  as a function of  $J_c$ . Here,  $f_{pulse}(t, \tau_p)$  is a pulse function that is 0 for  $t < 0$  and  $t > \tau_p$  and unity elsewhere. We assume  $M_s = 10^6$  A/m,  $\theta_{SH} = 0.3$ ,  $\alpha = 0.2$ ,  $d = 1$  nm and  $\vec{B} = (165$  mT) $\hat{x}$ . In this calculation, the anisotropy is fixed so the anisotropy field is  $\sim 0.6$  T without any external field. Yellow indicates the new equilibrium orientation points in the same direction as before the current pulse. Blue indicates switching.

### 7.2. Temperature Dynamics

Ultrafast heating of a magnetic material lead to temperature-induced changes to the magnetic moment and the interfacial anisotropy. We estimate the temperature response of the metal film in our experiments by solving the heat-diffusion equation

$$C \frac{dT}{dt} = \Lambda \frac{d^2T}{dx^2} + q(t) \quad (\text{eq.S4})$$

Here,  $T$  is the temperature rise above room temperature due to heating,  $C$  is the heat-capacity per unit volume,  $\Lambda$  is the thermal conductivity, and  $q(t)$  is the volumetric heating from either a laser or electrical pulse. Based on literature values of the heat-capacity of metals [1] and the thickness of each layer, we estimate an average value for  $C$  of the multilayer of  $2.6 \text{ J m}^{-3} \text{ K}^{-1}$  for our stack at room temperature. We fix  $\Lambda$  according to the Wiedemann-Franz Law  $\Lambda = L_0 T / \rho_e \sim 10 \text{ W m}^{-1} \text{ K}^{-1}$ , where  $\rho_e$  is the measured electrical resistivity of the film. For the optical experiments described in section 7.3., we assume  $q(t) = P(t) / (\pi w_0^2 d)$ , where  $P(t)$  is the laser power vs. time,  $w_0$  is the  $1/e^2$  radius, and  $d$  is the total film thickness of 16 nm. For electrical experiments, we set  $q(t) = \rho_e J^2(t)$ , where  $J(t)$  is the charge current density.

Solving Eq. (eq.S4) for  $T(t)$  requires boundary conditions. We assume an adiabatic boundary condition at the metal film surface. We assume the heat-current  $J_Q$  at the bottom of the metal film, is limited by the interfacial thermal conductance  $G_{int}$  between Ta and sapphire,

$$J_Q = G_{int} T(z = d). \quad (\text{eq.S5})$$

Typical values for the conductance between metal films and oxide substrates are 100-300  $\text{MW m}^{-2} \text{ K}^{-1}$  [2-4]. We treat  $G_{int}$  as a fit parameter and deduce  $G_{int} \sim 170 \text{ MW m}^{-2} \text{ K}^{-1}$ .

By using Eq. (eq.S4) to model the temperature response of the stack to heating, we are assuming that electrons, phonons, and spins are in thermal equilibrium with one another. Such an assumption is not always valid on picosecond time-scales, and nonequilibrium between thermal reservoirs can drive ultrafast magnetic phenomena [5]. In our experiments, nonequilibrium effects should be small due to the 4-6 picosecond pulse duration of the electrical experiments, together with the strong thermal coupling between electrons and phonons in the Co layer [6]. The picosecond time-scale for heating is much greater than the electron-phonon relaxation time in transition metals [7]. Therefore, we can estimate the nonequilibrium between electrons and phonons by assuming a quasi-steady-state condition where rate of heat absorption of electrons equals the rate of heat-loss to the phonons. In other words, we assume  $q(t) \sim g_{ep} \Delta T_{ep}(t)$ , where  $g_{ep}$  is the electron-phonon volumetric energy transfer coefficient [8], which we take from Ref. [6]. For a maximum electrical current density of  $6 \cdot 10^{13} \text{ A m}^{-2}$ , this estimate provides an upper bound for the nonequilibrium during our experiments of  $\Delta T_{ep}(t) \sim 15 \text{ K}$ .

### 7.3. Anisotropy Torques and Precessional Dynamics Caused by Ultrafast Heating

The anisotropy field and magnetization are both temperature dependent [9]. As a result, picosecond changes in the temperature of the Co film induce precessional dynamics [10], even in the absence of spin-orbit-torques or Oersted fields. To experimentally investigate the effect of temperature, we perform time-resolved magneto-optic Kerr effect measurements on the sample in the presence of an in-plane magnetic field. Prior to these time-resolved measurements, we orient the magnetic moment of the Cobalt with an out-of-plane magnetic field of 0.3 Tesla. After removing the out-of-plane magnetic field, we optical heat the sample surface with 250 fs duration pump pulses at a fluence of  $0.7 \text{ J m}^{-2}$ . The transient temperature response causes precessional dynamics. We track the resulting out-of-plane component of the magnetic moment by monitoring the polar Kerr angle with a time-delayed probe pulse. We repeat this experiment with varied in-plane magnetic fields.

The results of time-resolved magneto-optic Kerr measurements with an in-plane field of 0, 0.15, and 0.3 T are shown in Fig. S7. The lines are lines in Fig. S2 are best-fit model predictions for the data based on the LLG equations. We describe those predictions in more detail below.

Using an optical multilayer calculation like described in Ref. [11], we estimate the absorbed fluence per pump pulse is  $0.3 \text{ J m}^{-2}$ . This absorbed fluence will cause a per-pulse temperature rise of  $\sim 7 \text{ K}$ . Comparing this temperature rise to our experimental measurements of the resulting  $\Delta M_z$ , allows us to quantify  $dM_z/dT$ . The amplitude of precession of  $M_z(t)$  following heating provides information about  $dK_z/dT$ . The frequency and decay rate of precession allow us to determine the total anisotropy field and effective damping.

To theoretically quantify the effects of the temperature-evolution after optical heating we added temperature effects to Eq. (eq.S1-S3). We allow  $M_s$  and  $K_z$  in Eq. (eq.S1-S3) to evolve in time based on the predictions of our thermal model described in Eq. (eq.S4-S5). We follow Ref.[8], and assume the temperature dependence of the magnetization is well-described by

$$M_s(T) = M_s(0) [1 - (T/T_c)^{1.7}] \quad (\text{eq.S6})$$

$$K_z(T) = K_z(0) [M_s(T)/M_s(0)]^3 \quad (\text{eq.S7})$$

Here,  $T_c$  is the Curie temperature,  $M_s(0)$  is the magnetization at absolute zero, and  $K_z(0)$  is the anisotropy constant at absolute zero. We fix  $M_s(T = 300 \text{ K})$  to  $10^6 \text{ A/m}$  based on VSM measurements. We treat  $K_z(T = 300 \text{ K})$  as a fit-parameter. The precessional frequency in Fig. eq.S2 depends only on the magnetic moment and total anisotropy field. With  $M_s(300 \text{ K})$  fixed from VSM measurements, the only unknown parameter that effects the precessional frequency is  $K_z(300 \text{ K})$ . The best-fit value for  $K_z(300 \text{ K})$  is  $10^6 \text{ J m}^{-3}$ , corresponding to an out-of-plane anisotropy field of approx. 0.8 T. We fit for the effective value of  $\alpha$  in eq.S1 by matching model's prediction for the decay of oscillations to the data. We note that the effective  $\alpha$  includes effects such as inhomogeneous broadening [12]. The only remaining model parameter is  $T_c$ . The value of  $T_c$  determines  $dM_z/dT$  and  $dK_z/dT$  at room temperature. A best-fit to

our data in Fig. S2 yields  $T_c \sim 800$  K, in agreement with our extensive experience with similar samples grown in the same sputtering system. Then, eqs.S6-S7 predict  $dM_z/dT \sim -10^3$  Am<sup>-1</sup>K<sup>-1</sup> and  $dK_z/dT \sim -4 \cdot 10^3$  Jm<sup>-3</sup>K<sup>-1</sup>.

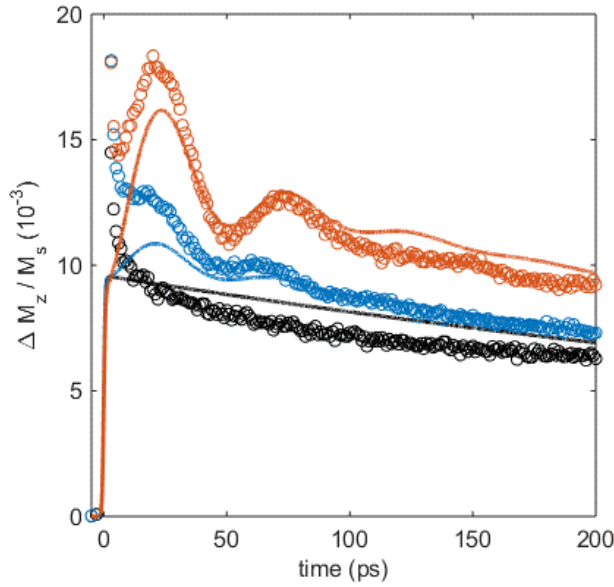


**Figure S7.** Time-resolve magneto optic Kerr effect of temperature induced dynamics of the sample. Markers are experimental data. Lines are LLG macrospin predictions with 0 (black), 0.15 (blue) and 0.3 T (orange) in-plane magnetic fields.

#### 7.4. Effect of Heating on Ultrafast SOT Dynamics

To evaluate the role of temperature rises on the switching dynamics, we use the model parameters described above, to estimate the change in dynamics that results from the addition of temperature-induced precessional dynamics. Figure S8 illustrates how temperature effects increase the amplitude of the electric-pulse induced dynamics and can aid switching.

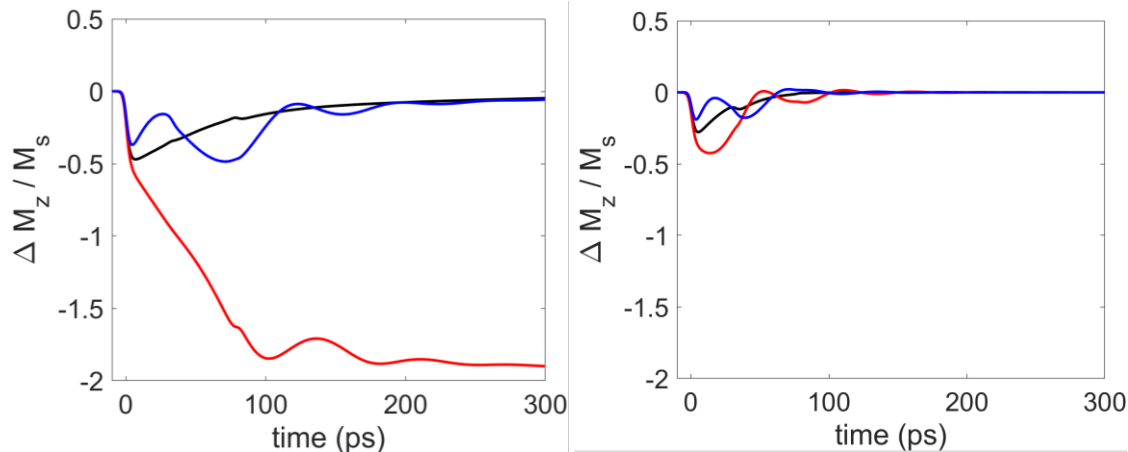


**Figure S8.** Switching dynamics predicted with a 6 ps pulse at  $J_c = 9.5 \cdot 10^{12}$  A/m<sup>2</sup>. Left plot includes thermal effects, whereas the right plot neglects them. We can clearly see that heating assists importantly the switching. Blue, red and black curves correspond to positive, negative and zero in-plane magnetic fields for the same given current polarity and initial out-of-plane magnetization. The reversal (crossing of zero) takes about 30ps in our simulations.

#### References:

1. Y. S. Touloukian (Editor), Recommended Values of the Thermophysical Properties of Eight Alloys, Major Constituents and their Oxides Thermophysical Properties Research Center, Purdue University, Lafayette, Indiana, February, 1966
2. Hopkins, P.E., Thermal transport across solid interfaces with nanoscale imperfections: Effects of roughness, disorder, dislocations, and bonding on thermal boundary conductance. ISRN Mechanical Engineering, 2013. 2013.
3. Wilson, R., B.A. Apgar, W.-P. Hsieh, L.W. Martin, and D.G. Cahill, Thermal conductance of strongly bonded metal-oxide interfaces. *Physical Review B*, 2015. 91(11): p. 115414.
4. Monachon, C., L. Weber, and C. Dames, Thermal boundary conductance: A materials science perspective. *Annual Review of Materials Research*, 2016. 46: p. 433-463.
5. Beaurepaire, E., J.-C. Merle, A. Daunois, and J.-Y. Bigot, Ultrafast spin dynamics in ferromagnetic nickel. *Physical review letters*, 1996. 76(22): p. 4250.
6. Verstraete, M.J., Ab initio calculation of spin-dependent electron–phonon coupling in iron and cobalt. *Journal of Physics: Condensed Matter*, 2013. 25(13): p. 136001.
7. Allen, P.B., Empirical electron-phonon  $\lambda$  values from resistivity of cubic metallic elements. *Physical Review B*, 1987. 36(5): p. 2920.
8. Wilson, R.B., Y. Yang, J. Gorchon, C.-H. Lambert, S. Salahuddin, and J. Bokor, Electric current induced ultrafast demagnetization. *Physical Review B*, 2017. 96(4): p. 045105.
9. Lee, K.-M., J.W. Choi, J. Sok, and B.-C. Min, Temperature dependence of the interfacial magnetic anisotropy in W/CoFeB/MgO. *AIP Advances*, 2017. 7(6): p. 065107.
10. Atxitia, U., O. Chubykalo-Fesenko, N. Kazantseva, D. Hinzke, U. Nowak, and R.W. Chantrell, Micromagnetic modeling of laser-induced magnetization dynamics using the Landau-Lifshitz-Bloch equation. *Applied physics letters*, 2007. 91(23): p. 232507.
11. Yang, Y., R.B. Wilson, J. Gorchon, C.-H. Lambert, S. Salahuddin, and J. Bokor, Ultrafast magnetization reversal by picosecond electrical pulses. *Science Advances*, 2017. 3(11).
12. Lattery, D.M., J. Zhu, D. Zhang, J.-P. Wang, P.A. Crowell, and X. Wang, Quantitative analysis and optimization of magnetization precession initiated by ultrafast optical pulses. *Applied Physics Letters*, 2018. 113(16): p. 162405.

